









# Mesoproterozoic surface oxygenation accompanied major sedimentary manganese deposition at 1.4 and 1.1 Ga

Sam C. Spinks<sup>1</sup>  | Erik A. Sperling<sup>2</sup>  | Robert L. Thorne<sup>1</sup>  | Felicity LaFountain<sup>1,3</sup>  |  
Alistair J. R. White<sup>1</sup>  | Joseph Armstrong<sup>1,4</sup>  | Martijn Woltering<sup>1</sup>  | Ian M. Tyler<sup>1,5</sup> 

<sup>1</sup>CSIRO Mineral Resources, Australian Resources Research Centre, Kensington, Western Australia, Australia

<sup>2</sup>Department of Geological Sciences, Stanford University, Stanford, California, USA

<sup>3</sup>School of Earth and Planetary Sciences, The Institute of Geoscience Research, Curtin University, Perth, Western Australia, Australia

<sup>4</sup>School of Geosciences, University of Aberdeen, Aberdeen, Scotland

<sup>5</sup>Centre for Exploration Targeting, School of Earth Sciences, University of Western Australia, Perth, Western Australia, Australia

## Correspondence

Sam C. Spinks, Teck Resources Ltd., 35 Ventnor Avenue, West Perth, Western Australia, Australia.  
Email: [sam.spinks@teck.com](mailto:sam.spinks@teck.com)

## Funding information

American Chemical Society Petroleum Research Fund; Australian Science and Industry Endowment Fund

## Abstract

Manganese (Mn) oxidation in marine environments requires oxygen (O<sub>2</sub>) or other reactive oxygen species in the water column, and widespread Mn oxide deposition in ancient sedimentary rocks has long been used as a proxy for oxidation. The oxygenation of Earth's atmosphere and oceans across the Archean-Proterozoic boundary are associated with massive Mn deposits, whereas the interval from 1.8–1.0 Ga is generally believed to be a time of low atmospheric oxygen with an apparent hiatus in sedimentary Mn deposition. Here, we report geochemical and mineralogical analyses from 1.1 Ga manganeseiferous marine-shelf siltstones from the Bangemall Supergroup, Western Australia, which underlie recently discovered economically significant manganese deposits. Layers bearing Mn carbonate microspheres, comparable with major global Mn deposits, reveal that intense periods of sedimentary Mn deposition occurred in the late Mesoproterozoic. Iron geochemical data suggest anoxic-ferruginous seafloor conditions at the onset of Mn deposition, followed by oxic conditions in the water column as Mn deposition persisted and eventually ceased. These data imply there was spatially widespread surface oxygenation ~1.1 Ga with sufficiently oxic conditions in shelf environments to oxidize marine Mn(II). Comparable large stratiform Mn carbonate deposits also occur in ~1.4 Ga marine siltstones hosted in underlying sedimentary units. These deposits are greater or at least commensurate in scale (tonnage) to those that followed the major oxygenation transitions from the Neoproterozoic. Such a period of sedimentary manganogenesis is inconsistent with a model of persistently low O<sub>2</sub> throughout the entirety of the Mesoproterozoic and provides robust evidence for dynamic redox changes in the mid to late Mesoproterozoic.

## KEYWORDS

atmospheric oxygenation, Capricorn Orogen, iron speciation, manganese, Mesoproterozoic, supergene ore deposits

This is an open access article under the terms of the [Creative Commons Attribution-NonCommercial-NoDerivs](https://creativecommons.org/licenses/by-nc-nd/4.0/) License, which permits use and distribution in any medium, provided the original work is properly cited, the use is non-commercial and no modifications or adaptations are made.

© 2022 CSIRO and The Authors. *Geobiology* published by John Wiley & Sons Ltd.

## 1 | INTRODUCTION

In ancient marine environments, oxidation of Mn(II) to Mn(III, IV) oxides, and thus deposition of sedimentary Mn, occurs at the redox interface between Mn(II)-bearing anoxic water and oxic waters in the presence of free O<sub>2</sub> or other reactive oxygen species (ROS) such as superoxide (Diem & Stumm, 1984; Geszvain et al., 2012; Hansel, 2017; Learman et al., 2011; Tebo et al., 2010). These reactions are bacterially mediated due to strong kinetic inhibitions (Hansel, 2017; Learman et al., 2011). Sedimentary Mn(III, IV) oxides may then be re-reduced to Mn(II) in the sediment subsurface, often via biologically mediated oxidation of organic matter (Lovley & Phillips, 1988; Maynard, 2010) or abiotically via oxidation of sulfides or ferrous Fe (Johnson, Savalia, et al., 2016; Van Cappellen et al., 1998). This reduced Mn in turn may react with dissolved carbonate to form Mn(II) carbonate deposits (Johnson, Webb, et al., 2016; Maynard, 2010; Roy, 2006; Wittkop et al., 2020) that can be preserved through geological time (Johnson, Webb, et al., 2016; Maynard, 2010; Planavsky, Asael, et al., 2014; Roy, 2006; Tsikos et al., 2003). These processes form the largest and most economically significant sedimentary Mn deposits in the ancient geological record.

Low-O<sub>2</sub> concentrations in surface environments during the Archean and throughout much of the mid-Proterozoic (reviewed by Lyons et al., 2014) allowed the development of a large dissolved Mn(II) reservoir in the oceans. Ultimately, surface oxygenation (Hodgskiss & Sperling, 2022; Lyons et al., 2014; Poulton et al., 2021) is hypothesized to have triggered the onset of oxidation of the Mn(II)-bearing anoxic oceans at the redoxcline, resulting in major sedimentary Mn deposition in the Paleoproterozoic (Johnson, Webb, et al., 2016; Maynard, 2010; Roy, 2006). Thus, enhanced periods of sedimentary Mn deposition are regarded as a strong indicator for oxidation of reduced Mn(II). An apparent pronounced hiatus in Mn deposition ~1.8–0.9 Ga, prior to the deposition of Neoproterozoic glaciogenic-related (Snowball Earth) Mn-Fe deposits (Freitas et al., 2021; Johnson, Webb, et al., 2016; Maynard, 2010; Roy, 2006), may indicate that low-O<sub>2</sub> conditions endured in surface environments throughout much of the late Paleoproterozoic and Mesoproterozoic (Cawood & Hawkesworth, 2014). Indeed, broadly reducing conditions throughout the Mesoproterozoic have been suggested in a range of other geochemical studies (Bellefroid et al., 2018; Cole et al., 2016; Crockford et al., 2018; Liu et al., 2021; Planavsky et al., 2018; Planavsky, Reinhard, et al., 2014). Conversely, a “Mn hiatus” during this time may theoretically reflect a fully oxygenated marine environment (Maynard, 2010; Roy, 2006), though independent geochemical evidence for this is lacking and is, therefore, considered unlikely. Recent geochemical studies have equivocally suggested the existence of at least transient oxidative Mesoproterozoic marine environments (Canfield et al., 2018; Diamond & Lyons, 2018; Gilleaudeau & Kah, 2015; Hardisty et al., 2017; Parnell et al., 2010, 2015; Sheen et al., 2018; Sperling et al., 2014; Zhang et al., 2016, 2017, 2018), yet clear lithological evidence such as major sedimentary Mn in rocks of that age remains elusive, other than a minor deposit in northern China deposited at 1.4 Ga (Fan et al., 1999; Su

et al., 2010). The discovery of major Mesoproterozoic sedimentary Mn deposits would, therefore, represent some of the most robust evidence to date for a relatively well-oxygenated ocean/atmosphere system during that time as well as help dispel the notion that the mid-Proterozoic was characterized by a stable and monotonous Earth system.

Here, we present new sedimentological, petrographic, and geochemical (major- and trace-element abundance, iron speciation, carbon isotope, and total organic carbon analysis) study of new drill cores from the Mesoproterozoic Ilgarari Formation, Western Australia, to understand the genesis of major surficial manganese deposits in the region and their implications for Earth history.

## 2 | GEOLOGICAL BACKGROUND

The Proterozoic Edmund and Collier Basins of Western Australia, which host the sedimentary rocks of the Bangemall Supergroup (Cawood & Tyler, 2004; Cutten et al., 2016; Martin et al., 2008; Martin & Thorne, 2004), extend for over 500 km E-W and up to 475 km N-S in the Capricorn Orogen (Figures 1 and 2). These basins formed following the collision of the Archean Pilbara and Yilgarn Cratons with the Paleoproterozoic Glenburgh Terrane between 2.21–1.95 Ga, collectively forming the West Australian Craton (Cawood & Tyler, 2004). The Edmund Basin formed during relaxation and extension of the orogenic belt following the 1.82–1.77 Ga Capricorn Orogeny and the 1.68–1.62 Ga intraplate Mangaroon Orogeny (Sheppard et al., 2005), depositing the sedimentary rocks of the 1.62–1.45 Ga Edmund Group in a half graben structure. The Edmund Group was deformed locally to greenschist facies during the 1.32–1.17 Ga Mutherbukin Tectonic Event, prior to the formation of the Collier Basin and unconformable deposition of the younger 1.17–1.11 Ga (Armandola et al., 2018) Collier Group and the contemporaneous lateral equivalent Manganese Group (Grey et al., 2010). The Manganese Group is situated in the northern sub-basin of the Collier Basin, at the eastern margin of the Pilbara Craton (Figures 1 and 2). This study focuses on stratiform-sedimentary Mn deposits of the ~1.45 Ga Ullawarra Formation of the Edmund Group and the ~1.11 Ga Ilgarari Formation in the Collier Group, deposited in the southern sub-basin of the Collier Basin (Figures 1 and 2).

### 2.1 | Proterozoic manganese mineralization in the Pilbara Manganese Belt

Hundreds of Mn deposits, prospects and occurrences have been identified in the Neoproterozoic–Paleoproterozoic Hamersley Basin in the Pilbara Craton and the numerous Paleo-Mesoproterozoic basins that occur in a belt throughout the Capricorn Orogen (Figure 1), which is herein referred to as the *Pilbara Manganese Belt* (PMB). The Mesoproterozoic Edmund and Collier basins host numerous surficial stratiform Mn deposits and mineral occurrences that are expressed at the surface as massive supergene caps of Mn oxide that

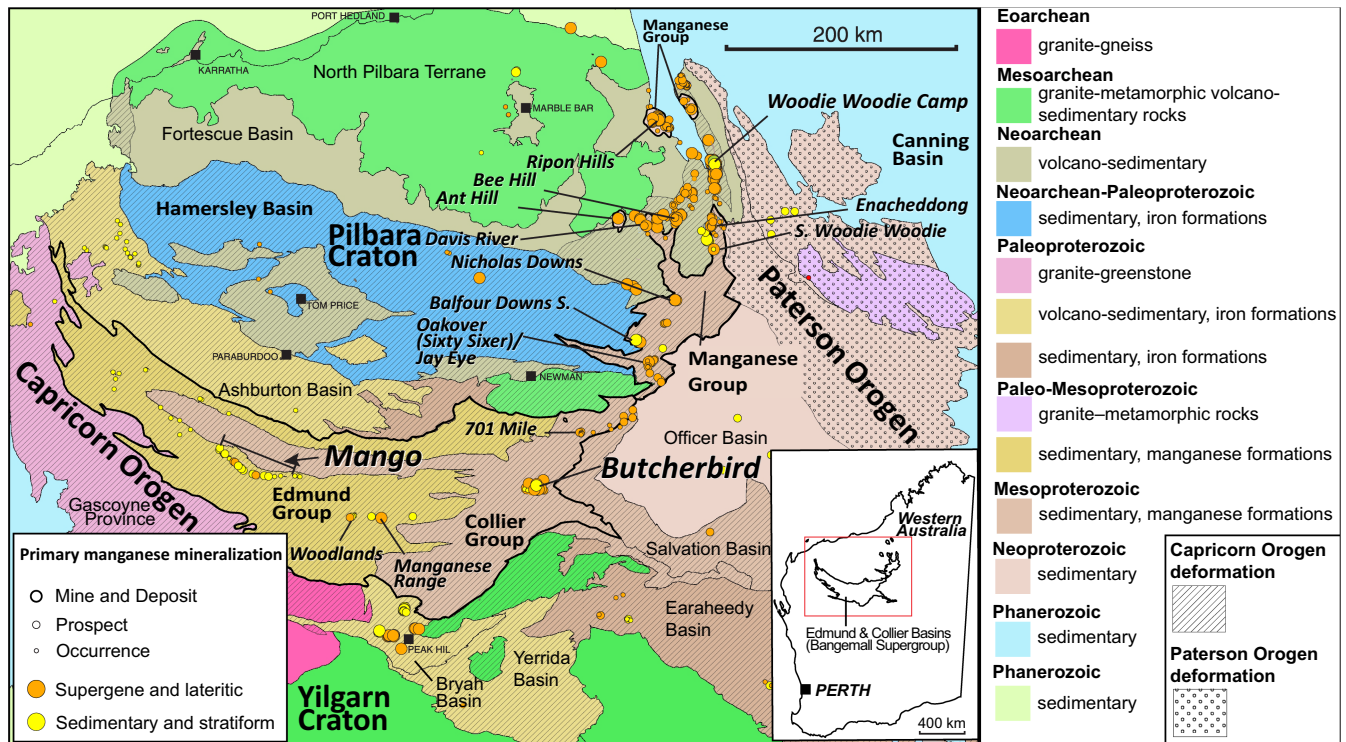


**FIGURE 1** Summary geological map of the major tectonic units and sedimentary basins in NW Western Australia, with supergene-lateritic Mn and sedimentary-stratiform Mn deposits, prospects and occurrences (see [Supplementary Information](#) for data sources). Inset map shows locations of the Edmund and Collier Basins within Western Australia. The Edmund, Collier and Manganese groups comprise the Bangemall Supergroup. The Mango deposits of the (1.4 Ga) Edmund Group, the Butcherbird deposit in the late (1.1 Ga) Mesoproterozoic Collier Group, and the Woodie Woodie deposits (potentially) in the Neoproterozoic (0.83 Ga) Tarcunyah Group, respectively, are highlighted. Numerous Mn deposits and prospects occur throughout the region, but are interchangeably reported as “supergene” and/or “sedimentary,” while the underlying unweathered rocks have never been studied and their formation mechanisms remain unknown.

formed in situ (this study) by the intensive oxidative weathering of the Proterozoic stratigraphy, resulting in alteration of detrital silica, alumina and resistate phases and minimal loss of Mn and Fe. This process results in relative enrichment in Mn and Fe without addition of metals from external sources.

In the main basin (south), stratiform deposits occur in the ~1.45 Ga marine siltstones of the Ullawarra Formation in the Edmund Group (e.g. the Mango deposits), and the ~1.11 Ga Ilgarari Formation of the Collier Group (e.g. the Butcherbird Deposit; [Figures 1 and 2](#)). These deposits are largely unstudied due to a paucity of unweathered rock at the surface, but they are generally assumed to be sedimentary in origin, given their planar stratiform geometry in otherwise largely non-deformed rocks. Other supergene Mn deposits of non-sedimentary origin occur in the Edmund Group, such as the Woodlands and Manganese Range Mn deposits ([Figure 1](#); [Pirajno et al., 2016](#)), which likely formed by hydrothermal alteration of carbonate during the base metal ore formation of the nearby Mesoproterozoic Abra Pb-Zn deposit ([Spinks et al., 2017](#)).

In the northern sub-basin that is dominated by the Manganese Group of the Collier Basin, manganiferous siltstone packages are also expressed at surface as hundreds of economic stratiform in situ supergene Mn oxide deposits and prospects ([Figure 1](#)). These include major deposit projects such as Oakover (Sixty Sixer), Ripon

Hills, Bee Hill, Ant Hill, Enacheddong, Davis River, Nicholas Downs and Balfour Downs. Resource estimates from these deposits are explained in [Appendix S1](#). The mineralized stratiform deposits of the major Woodie Woodie mining camp that overlie manganiferous vein networks within the Neoproterozoic Carawine Dolomite (lower Hamersley Group) basement ([Jones et al., 2013](#)) ([Figure 1](#), [Appendix S1](#)) have also been recognized as sedimentary in origin, purportedly also part of the Manganese Group ([Jones, 2017](#)). The host unit to these deposits was interpreted as the Manganese Group in [Jones et al. \(2013\)](#). However, following mapping by the Geological Survey of Western Australia incorporating stromatolite biostratigraphy, the host unit was formally assigned to the Waltha Woorra Formation, part of the ~0.83 Ga Neoproterozoic Tarcunyah Group deposited in the northwest Officer Basin ([Figure 1](#); [Grey et al., 2005](#)). It is noted that quantitative geochronological data for the unit in that area have not yet been documented. Therefore, while there is significant stratiform Mn deposition in the Manganese Group of the northern Collier Basin, including north of Woodie Woodie, the presence of sedimentary Mn in the 1.1 Ga Manganese Group within the giant Woodie Woodie camp is uncertain.

Additionally, significant stratiform Mn deposits occur in the Paleoproterozoic Bryah (2.0–1.9 Ga) and Earaheedy (2.0–1.6 Ga)

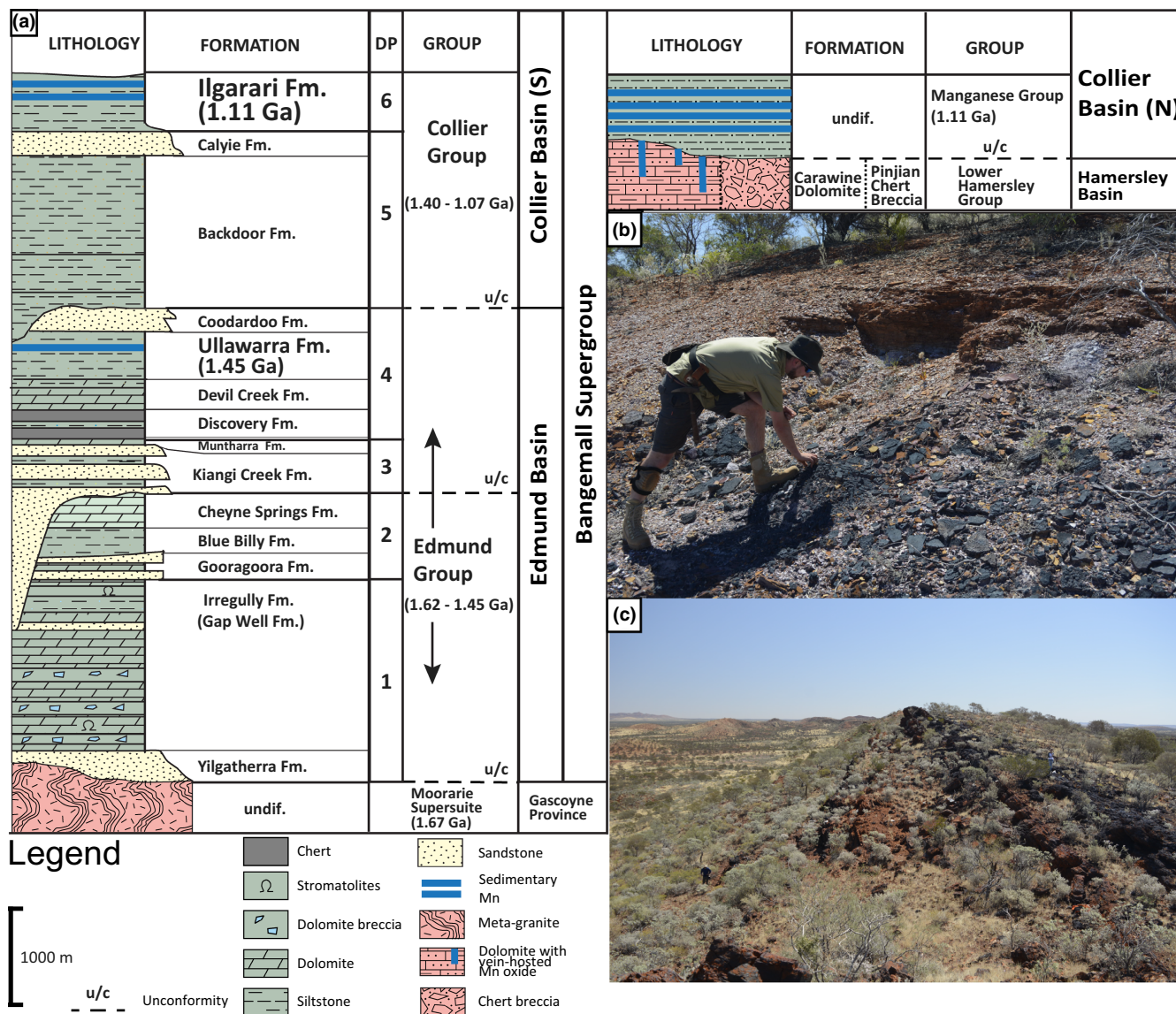


**FIGURE 2** (a) Simplified geological log of the Proterozoic Bangemall Supergroup (Edmund and Collier basins) of Western Australia showing the occurrences of stratiform-sedimentary manganese deposits. The Edmund and Collier groups are subdivided into six “Depositional Packages” (DP), which mark major erosive and depositional surfaces, and further into individual formations. The late Mesoproterozoic (1.11 Ga) Collier Group (Ilgarari Formation) and Manganese Group are part of the Collier Basin and occur in the south and north sub-basins, respectively. The ~1.45 Ga Ullawarra Formation was deposited in the Edmund Basin. Modified after Martin and Thorne (2004). (b) Outcrop of stratiform supergene Mn oxide ore sequence at the Butcherbird deposit (Ilgarari Formation). (c) Outcrop of the Mango 4 deposit, part of a ~90 km long exposure of stratiform supergene Mn oxide ore sequence hosted in the Ullawarra Formation.

basins on the northern margins of the Yilgarn Craton within the Capricorn Orogen (Figure 1).

This study focuses on the recently discovered stratiform Mn mineralization at the giant Butcherbird deposit, which offers an excellent opportunity to investigate sedimentary Mn deposition, and new nearby drill cores (e.g. drill hole DD14IL014) have provided the first ever access to unweathered samples of the underlying stratigraphy. The Butcherbird deposit is currently the only Mn deposit in the Edmund and Collier groups with an Australian JORC (Joint Ore Reserves Committee) compliant mineral resource estimate, which is currently at least 263 million tons (Mt) of Mn (Appendix S1), ranking it among the largest in the world. The contemporaneous stratiform

Mn deposits with JORC resources in the Manganese Group to the north of the Butcherbird deposit have combined JORC Resources of 364.05 Mt Mn. These combined with Butcherbird add to a JORC Resource of (at least) 627 Mt of Mn in the Collier Basin. These JORC Resources are outlined in Appendix S1.

## 2.2 | Edmund Group (Ullawarra Formation)

The Edmund and Collier groups are subdivided into six “Depositional Packages” that mark major tectonic and depositional surfaces in the development of the basins. This nomenclature framework and

a detailed overview of basin development are provided by Martin and Thorne (2004) and Martin et al. (2008). The stratigraphy is further divided into 14 lithostratigraphic formations (Figure 2). Depositional Package 4 (a focus of this study) is defined by the basal conglomerates of the Discovery Formation and the overlying pyritic black mudstones, which mark the beginning of a basin-wide transgression after ~1.59 Ga (Wingate et al., 2021). These are overlain by the shallow carbonate platform facies of the Devil Creek Formation. The Ullawarra Formation, the unit that is the focus of study in the Edmund Group, and the conformably overlying Coodardoo Formation are the uppermost units in the Edmund Group. Together they have a poorly constrained minimum depositional age of 1.45 Ga (Thorne, 2018). The Ullawarra Formation ranges between 100 and 600 m thick, increasing to the south over the Talga Fault, and is composed predominantly of marine (early diagenetic) dolomitic siltstone, with lesser dolostone, fine sandstone and chert. The lithologies are described in detail in Martin et al. (2005), and were deposited in a progressively deepening intracontinental shelf environment during a major marine transgression (Martin & Thorne, 2004). The Coodardoo Formation is interpreted to represent a deep marine turbiditic sandstone sequence (Martin & Thorne, 2004). No drill core material of the Ullawarra Formation was available in this study. Outcrops observed at the studied sections (the Mango deposits, Figure 1) form a regional ridge that extends ~90 km along strike and is made up entirely of interbedded weathered Mn oxide rich siltstones and red ferruginous siltstones with a prominent massive Mn oxide (ore) cap at the top of the sequence (Appendix S1).

### 2.3 | Collier Group (Ilgarari Formation)

The 1.11 Ga (Armandola et al., 2018) Ilgarari Formation of the Collier Group (Figures 1 and 2) is a ~700–1500 m thick sequence of marine siltstones and pyritic carbonaceous mudstones with minor fine sandstones and carbonates that forms the uppermost package in the Collier Basin. These were deposited in a progressively deepening intracontinental shelf environment during a major marine transgression (Martin & Thorne, 2004). The Ilgarari Formation lithologies intersected in drill hole DD14IL014 (Figure 3) comprises basal interbedded white sandstone deposited in a shallow deltaic or estuarine environment, overlain by ~400 m of interbedded shelf siltstone and carbonaceous mudstone that record a deepening of the basin. The siltstones and mudstones are locally pyritic and are uniformly planar laminated through the entire section with no soft-sediment deformation, indicating deposition on a stable shelf at depth, well below the storm wave base. The upper siltstones are characteristically pink-grey in color, planar laminated, and with up to 15 cm thick bedded accumulations of kutnohorite-rhodochrosite Mn carbonates. These are interbedded with black carbonaceous and pyritic mudstones and siltstones at the decimeter scale (see Appendix S1 for core imagery).

## 3 | MATERIALS AND METHODS

### 3.1 | Whole rock geochemistry

Analysis for major elements (oxides)  $\text{Al}_2\text{O}_3$ , CaO, Fe,  $\text{K}_2\text{O}$ , MgO, MnO,  $\text{Na}_2\text{O}$ ,  $\text{P}_2\text{O}_5$ ,  $\text{SiO}_2$ ,  $\text{TiO}_2$ , and LOI was performed by LabWest Minerals Analysis using their in-house method AF-03. This method gives total recovery of major rock-forming metals. A 0.1 g portion of the sample is fused with a lithium metaborate/tetraborate flux at 1000°C. The resulting bead is dissolved in dilute (2%) nitric acid, with tumbling. Solutions are then analyzed by ICP-Emission Spectrometry (Perkin-Elmer Optima 7300DV) for determination of the desired analytes. Loss-on-ignition is performed gravimetrically, with ignition of a separate 1 g sample portion at 1000°C for 30 min. Elements are reported as oxides at percent level concentrations.

Analysis for minor and trace elements was performed by LabWest Minerals Analysis using their in-house method, MMA-04\*. This method gives almost total recovery of all but the most resistate minerals. All elements are presented at ppm concentration, apart from Re, which was measured at ppb level. About 0.1 g of sample is digested in a mixture of hydrofluoric, nitric and hydrochloric acids in sealed digestion vessels for 60 min, using an Anton-Paar MW3000 microwave digestion system. The digestion takes place at a temperature of approximately 160°C and 16 bar pressure. After addition of boric acid to neutralize remaining hydrofluoric acid, the solutions are made to volume with deionized water. Internal standards are added to the solutions at the digestion stage. The solutions are then analyzed by ICP-Mass Spectrometry (Perkin-Elmer Nexion 300Q) and ICP-Emission Spectrometry (Perkin-Elmer Optima 7300DV) for determination of the desired analytes. Information on standards and precision can be found in the QA/QC tab of the supplementary data file (Tables S1 and S2).

### 3.2 | Iron speciation

Samples for iron speciation were first analyzed using the chromium reduction of sulfur method (Canfield et al., 1986). Approximately 0.2–0.4 grams of sediment was added to a reaction flask, the flask purged of air with nitrogen gas, and 20 ml of 1 M chromous chloride, acidified to 0.5 N HCl, was added to the reaction vessels after 20 ml of 6 N HCl. These flasks were heated to near-boiling for 2 h, and resulting sulfide gas was trapped in a zinc acetate trapping solution. Pyrite contents (and iron in pyrite, via a stoichiometric calculation) were calculated following gravimetric measurement. Sequential iron extraction of iron in carbonates (extracted using a 48-h sodium acetate extraction at 50°C), iron oxides (extracted using a 2-h sodium dithionite extraction), and mixed-valence phases such as magnetite (extracted using a 6-h ammonium oxalate extraction) followed the protocol of Poulton and Canfield (2005). The iron extracted by these sequential extractions was measured using the ferrozine spectrophotometric method of Stookey (1970).

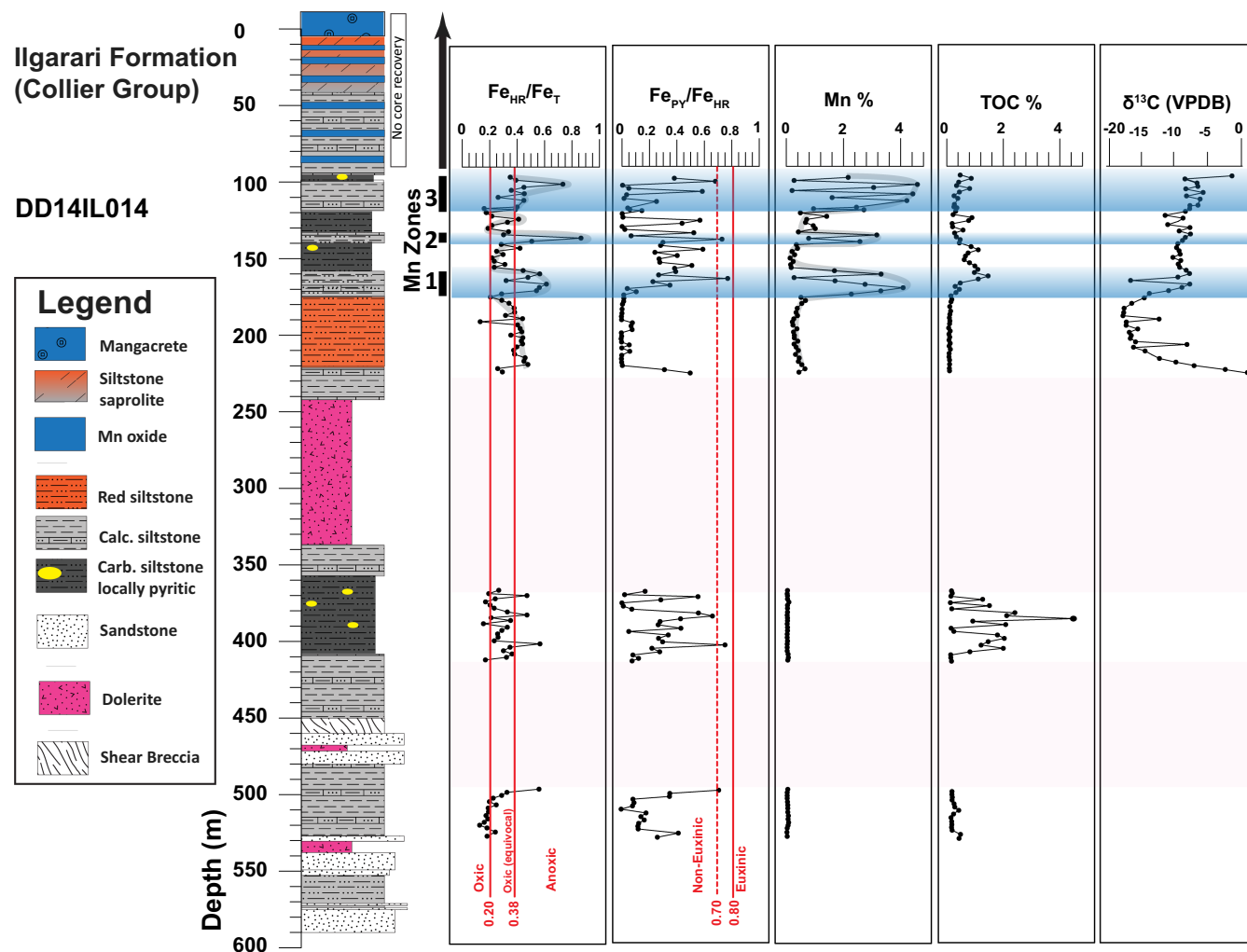


**FIGURE 3** Simplified geological log of the Ilgarari Formation (Collier Group) as intersected in drill core DD14IL014, with downhole plots of  $Fe_{HR}/Fe_T$ ,  $Fe_{PY}/Fe_{HR}$ , Mn (wt. %), TOC (wt. %) and C isotope values. Manganiferous beds and corresponding Fe data in Mn zones 1–3 are highlighted by blue bars, and the broad trend of Mn enrichments is outlined by a grey line for clarity. The pink shaded areas show depths where no samples were collected, i.e. from the dolerite sills.

Detailed estimates of precision for these methods can be found in the supplement of Sperling et al. (2021); samples during this study were run alongside the same set of internal lab standards with consistent results.

### 3.3 | Carbonate carbon isotopes and total organic carbon

Carbonate carbon isotope analyses were conducted at the Commonwealth Scientific and Industrial Research Organization (CSIRO) NGL Lab, Australian Resources Research Centre (ARRC) on a Thermo Fischer Scientific MAT253 Isotope Ratio Mass Spectrometer with dual inlet connected to a Gasbench II. During each batch run, a calibration series is run at the start, middle, and end, producing a calibration to transform the measured isotope readings to the VPDB scale. The carbonate standards utilized for the calibration process are standards IAEA-603 and IAEA-CO8

and the internal/lab CSIRO carbonate standard (CS1), which is calibrated to the VPDB scale ( $-13.46\%$  for C) through an inter-lab comparison.

Analysis for Total Organic Carbon was performed at CSBP Laboratories, Bibra Lake, Western Australia under subcontract by LabWest Minerals Analysis' in-house method code, TOEC. The sample is leached in dilute hydrochloric acid (by LabWest) to remove carbonates. After drying, the residue is determined for total carbon content by Leco analyzer (CSBP Laboratories, Bibra Lake, WA). The sample residue is introduced to the Leco combustion furnace in a ceramic crucible and heated to  $1350^{\circ}C$  in a stream of pure oxygen. Under these conditions, all common carbon species are decomposed to carbon dioxide, which is evolved from the sample and carried in the combustion gas stream through infrared absorption cells. Integrated infrared absorbance by  $CO_2$  from the sample is compared to concentration/absorbance (calibration) curves generated by samples of known carbon content, and the concentration in sample is thus determined.

### 3.4 | Quantitative petrography (mineral identification)

High-resolution element mapping and semi-quantitative mineralogy was determined using a Zeiss Ultra Plus field emission gun Scanning Electron Microscope (FEG-SEM), fitted with a Bruker XFlash 6 energy-dispersive spectrometer at the CSIRO Australian Resource Research Centre (ARRC) Advanced Characterization Facility in Perth, Australia. Samples were mounted on slides and analyzed by energy-dispersive X-ray spectroscopy at ~6 mm working distance. Standard analytical conditions were an accelerating voltage of 10 to 20 kV and a beam current of 690 pA. Data were collected and processed with the Bruker Esprit Quantax software package.

Quantitative mineral chemical data were obtained using a Tescan Mira3 field emission gun scanning electron microscope (FEG-SEM) fitted with an Oxford Instruments X-MaxN energy-dispersive spectrometer at the CSIRO Australian Resources Research Centre (ARRC) Advanced Resource Characterization Facility, Perth, Australia. Operating conditions were an accelerating voltage of 15 kV, a beam current of 2.0 nA, and a live count time of 100 s. Elemental calibrations were made against a range of natural mineral standards, an XPP matrix correction procedure was used, and count rate was calibrated using a pure cobalt metal standard. Data were collected and processed using the Oxford Instruments AZtec software package.

Automated mineralogy scanning was performed using a Tescan Integrated Mineral Analyzer (TIMA) scanning electron microscope (SEM) to precisely detect major and minor minerals that can be problematic and time consuming to be identified by conventional logging and conventional petrographic studies. This method produced detailed mosaics of samples, allowing textural and mineralogical information to be rapidly investigated on individual samples.

## 4 | RESULTS

### 4.1 | Manganiferous stratigraphy, mineralogy and textures

The siltstones intersected in drill core DD14IL014 display layers of unweathered Mn carbonates millimeters to several centimeters in thickness, with interbedded pyritic siltstones. Three broad horizons of manganiferous siltstones tens of meters in thickness can be identified, herein referred to as Mn Zones 1–3 in stratigraphic order (bottom to top). It is noted though that numerous thick beds of weathered (oxidized) Mn oxide overlie these, forming a massive supergene Mn oxide cap closer to the main ore deposit (Appendix S1), representing the presence of more manganiferous siltstone horizons above the sampled interval. Between the Mn Zones there are beds of black pyritic siltstones. Figure 3 shows detailed lithology and downhole geochemical plots with MnO concentrations up to 4.57% from systematic sampling every 6 m in carbonate-bearing beds of Mn Zones 1–3. Full geochemistry data is available in Table S1. Quantitative petrographic analyses of these rocks show that they contain zoned

Mn-carbonate intragranular cements and clusters within locally pyritic siltstone that are characterized by Ca–Mn-bearing ankerite  $[\text{Ca}(\text{Mg}, \text{Fe}^{2+}, \text{Mn}^{2+})(\text{CO}_3)_2]$ , kutnohorite  $[\text{Ca}, \text{Mn}^{2+}(\text{CO}_3)_2]$ , and Mn-bearing siderite  $[\text{Fe}^{2+}(\text{Mn}^{2+})\text{CO}_3]$  with localized ferroan-calcian rhodochrosite  $[\text{Mn}^{2+}\text{CO}_3]$  (Figure 4; Appendix S2 and Table S2). The ankerite-kutnohorite clusters commonly have a distinctive rhombic geometry and are porous (Figure 4c), implying possible replacement, or ankeritization of original early diagenetic-syngenetic dolomite in the presence of porewater Mn(II). Siderite rims, however, do not display replacement textures and have well-defined boundaries, suggesting they possibly precipitated as overgrowths. Sparse pyrite occurs in most thin sections and appears to be very early diagenetic in origin. Euhedral pyrite grains are observed to have been overgrown or enveloped by later carbonate (Figure 4a,b), demonstrating their presence before Mn carbonate precipitation. A final paragenetic sequence of (1) pyrite (2) Mn-ankerite, (3) kutnohorite (+rhodochrosite), (4) Mn-siderite is observed consistently throughout the Mn zones. This sequence is most clearly demonstrated in Figure 4c.

Outcropping siltstones below the supergene Mn oxide ore cap in the *Mango 4* deposit hosted in the Ullawarra Formation are partially weathered and were measured to have up to 15% MnO. XRF scanning of samples of these siltstones show that they host millimeter-sub millimeter scale planar bedded Mn oxide laminae consisting predominantly of cryptomelane  $\text{K}(\text{Mn}_7^{4+}\text{Mn}^{3+})\text{O}_{16}$  (Appendix S2).

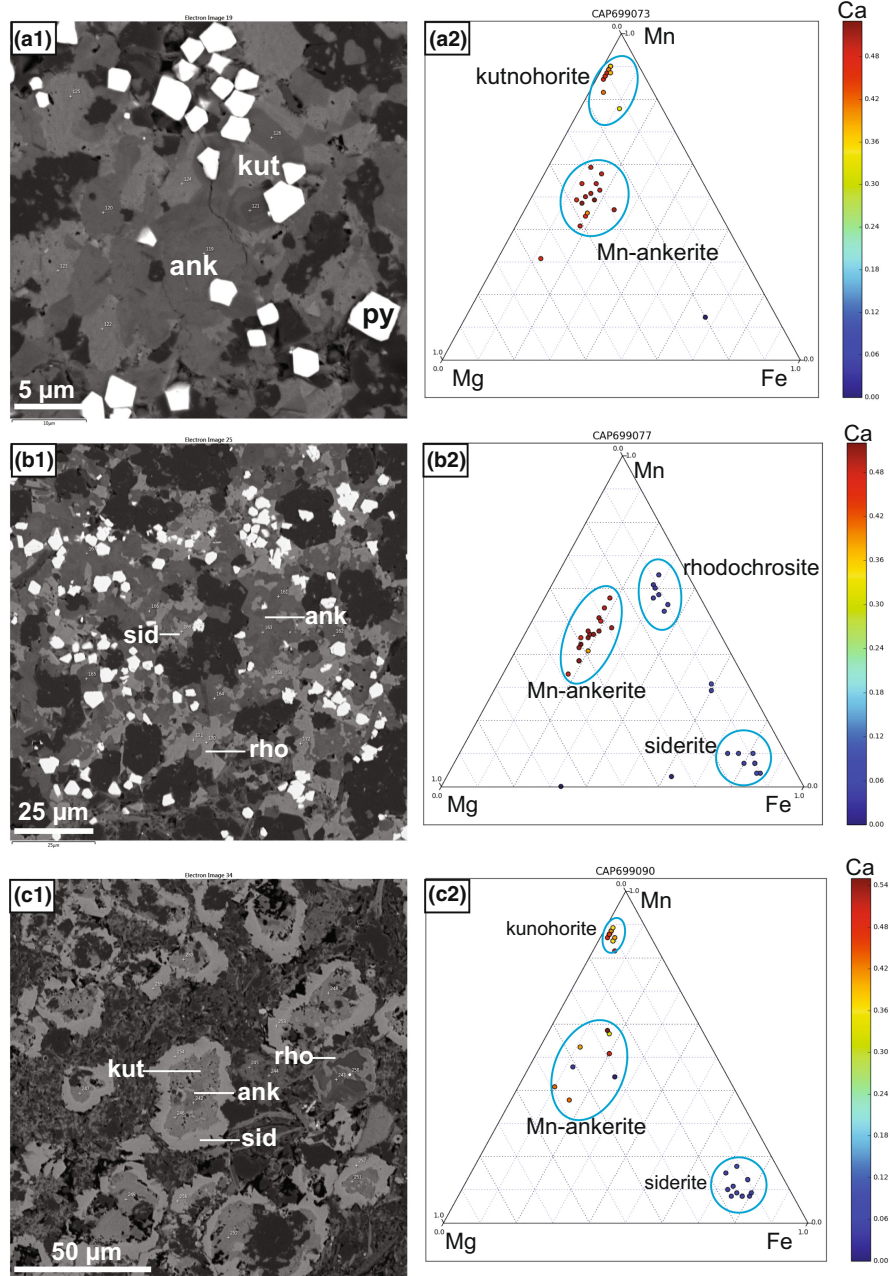
### 4.2 | Carbon isotopes

Carbonate carbon isotope analysis of the Ilgarari samples, including Mn carbonate-bearing and barren lithologies, was performed to determine the source of the carbon (seawater carbonate or organic carbon) and the reduction pathway. The manganiferous carbonate samples (>1.4% MnO) have  $\delta^{13}\text{C}_{(\text{carbonate})}$  values from  $-1.33$  to  $-16.62\text{‰}$  (VPDB), while non-manganiferous siltstones in the section have a similar spread of light values, as low as  $-17.9\text{‰}$  (Figures 4 and 5).

### 4.3 | Bottom water redox state

Iron speciation was performed to track the redox state of the water column overlying the investigated Ilgarari Formation sediments. Sediments deposited under modern oxygenated water columns have low abundances of highly reactive iron ( $\text{Fe}_{\text{HR}}$ ) relative to total iron ( $\text{Fe}_{\text{T}}$ ), reflected by  $\text{Fe}_{\text{HR}}/\text{Fe}_{\text{T}}$  ratios  $<0.38$  (Raiswell & Canfield, 1998). Sediments deposited under anoxic water columns are enriched in highly reactive iron (i.e.,  $\text{Fe}_{\text{HR}}/\text{Fe}_{\text{T}} > 0.38$ ), although under conditions of rapid sedimentation, such as in turbidites, these authigenic  $\text{Fe}_{\text{HR}}$  enrichments may be masked. In modern anoxic turbidites,  $\text{Fe}_{\text{HR}}/\text{Fe}_{\text{T}}$  ratios can reach values as low as 0.2 (Raiswell & Canfield, 1998; Sperling et al., 2016), and thus values 0.2–0.38 are considered equivocally oxic. The proxy can also distinguish between anoxic conditions that are ferruginous, or non-sulfidic ( $\text{Fe}_{\text{py}}/\text{Fe}_{\text{HR}} < 0.7$ ), versus euxinic, with

**FIGURE 4** Scanning electron microscope backscattered electron images of Mn carbonates in the Ilgarari Formation from drill core (DD14IL014), and corresponding ternary plots of quantitative atomic weight % data showing ideal compositions for the Mn carbonate minerals in the solid solution series. (a, b) Ankerite (ank) surrounded by later kutnohorite (kut), which is locally surrounded by Mn-rich siderite (sid) or rhodochrosite (rho). All Mn carbonate minerals have precipitated around earlier pyrite (py). (c) Clusters of these minerals, clearly demonstrating the paragenetic sequence, with localized rhodochrosite. (a) shows localized rhodochrosite (rho) while (b) shows localized pyrite (Py). All quantitative mineralogy data is expressed in the accompanying solid solution ternary diagrams a<sup>2</sup>, b<sup>2</sup>, c<sup>2</sup>.



free sulfide ( $Fe_{py}/Fe_{HR} > 0.7-0.8$ ), by considering the proportion of sulfidized versus unsulfidized reactive iron (Poulton & Canfield, 2011; Raiswell et al., 2018). Iron speciation does rely on identifying enrichments in highly reactive iron as a signature of anoxia, and there are situations in which these enrichments do not arise despite anoxic water-column conditions (discussed by Chen et al., 2020 with respect to the mid-Proterozoic). None of these processes, however, would be expected to occur cyclically in our studied core.

In the shallow facies (~525–360 m core depth) of the lower Ilgarari Formation,  $Fe_{HR}/Fe_T$  ratios appear variable, fluctuating from  $<0.20$  to  $>0.38$ , with  $Fe_{py}/Fe_{HR}$  ratios of close to 0.8 corresponding with highest  $Fe_{HR}/Fe_T$  ratios (Table S2). In the upper Mn-bearing section (~170–90 m core depth)  $Fe_{HR}/Fe_T$  ratios of ~0.20 (oxic and equivocal oxic interpretive fields) are observed at the bases of Mn Zones 1–3.

The  $Fe_{HR}/Fe_T$  ratios increase to  $>0.38$  (anoxic field) corresponding with the onset of enhanced Mn concentrations (Figure 3). Maximum  $Fe_{HR}/Fe_T$  ratios in the Mn zones 1–3 correlate with the highest Mn concentrations, and as the Mn concentrations decrease up section from the maxima in each zone, so do the  $Fe_{HR}/Fe_T$  ratios return back to values in the oxic ( $<0.2$ ) or equivocal oxic ( $<0.38$ ) interpretive fields. This trend is highlighted by the grey maximum value bars in (Figure 3). The  $Fe_{py}/Fe_{HR}$  ratios in Mn Zones 1–3 loosely follow this trend, with the highest values ( $>0.7$ ) corresponding with the peak Mn concentrations and generally high  $Fe_{HR}/Fe_T$ , and the lowest corresponding with low Mn concentrations and  $Fe_{HR}/Fe_T$  ratios. The majority of Mn-rich samples were, therefore, likely deposited under anoxic ferruginous bottom water conditions (high  $Fe_{HR}/Fe_T$  ratios), despite a few plotting as equivocally euxinic, which is also evident by



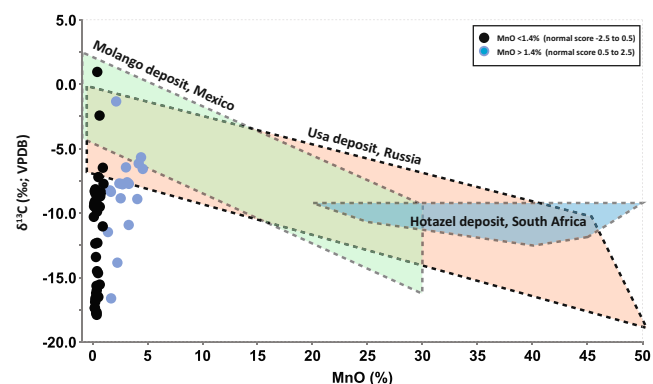


**FIGURE 5** Cross plot showing MnO concentrations versus  $\delta^{13}\text{C}_{(\text{carbonate})}$  data from the Ilgarari Formation, showing incorporation of isotopically light carbon into Mn carbonates. Approximate spread of data for sedimentary Mn deposits with an organic matter oxidation component are shown, Molango deposit (Okita et al., 1988), Usa deposit (Kuleshov & Bych, 2002) and the Hotazel deposit (Tsikos et al., 2003). Note that our unweathered drillcore samples from the Ilgarari Fm have relatively low manganese concentrations because they occur below the layers that formed the surficial supergene-enriched ore-grade deposits.

the presence of pyrite in some petrographic analyses (Figure 4). The predominance of anoxic and (mostly) non-sulfidic conditions in anoxic waters overlying the Ilgarari Formation is supported by muted enrichments in Mo, which requires the presence of sulfide in order to be sequestered in the sediment (Scott & Lyons, 2012). Molybdenum concentrations in Ilgarari samples average 2.2 ppm ( $\pm 4.5$  ppm), with a maximum of 23.3 ppm.

Recently, two studies have added complexity to the interpretation of iron extracted during the oxalate step (especially as measured here). First, Slotznick et al. (2020) have suggested that samples with high amounts of oxalate-extractable iron may actually be extracting iron-rich clays such as berthierine and chamosite rather than magnetite. Ilgarari Formation samples between 170–96 m depth in core have Fe-oxalate values of 0.77 wt. percent ( $\pm 0.69$  wt. percent 1 SD, maximum 4.17 wt. percent). On average, the Fe-oxalate pool comprises 29% of the total FeHR pool ( $\pm 13\%$ , maximum 56%). Although such values are not uncommon in Proterozoic shales (Slotznick et al., 2020), they are higher than most samples of any age. If these iron-rich clays are forming due to interactions with anoxic and iron-rich porewaters or water columns (Slotznick et al., 2020) this would not change the interpretive result, although the lack of understanding of the mineralogical source of oxalate-extractable iron would introduce ambiguity into these results. Notably, though, the most significant FeHR pool is Fe-acetate (average 35%, [ $\pm 13\%$ , maximum 58%]), and given that the formation of iron carbonates is a hallmark of ferruginous bottom waters (Canfield et al., 2008), we believe that the interpretation of ferruginous conditions for the Mn zones remains robust. Second, Alcott et al. (2020) recently evaluated different iron speciation extraction procedures and determined that ferrozine spectrophotometry, as conducted here, likely underestimates the Fe-oxalate pool by ~20% compared to other methods

such as AAS or ICP-OES (see extended discussion in supplement of Sperling et al. (2021)). Increasing our Fe-oxalate values by 20% will raise FeHR/FeT values by 0.017, on average. This does not change the observation that FeHR/FeT values are generally  $>0.38$  in the manganese zones and below this threshold between these zones. Increases to oxalate-extractable iron values would also reinforce the conclusion that anoxic bottom waters were ferruginous rather than euxinic.

## 5 | DISCUSSION

### 5.1 | Biologically mediated oxidation of organic carbon

The range of Mn carbonate minerals present in the 1.11 Ga Ilgarari Formation, and their textures, are comparable with other sedimentary Mn deposits from the ancient record such as the examples shown in Johnson, Webb, et al. (2016). This is consistent with a model of Mn deposition via either primary Mn carbonate precipitation or reduction of Mn oxides in the sedimentary package. These deposits are well-established as sedimentary in origin (e.g. Johnson et al., 2013; Johnson, Webb, et al., 2016; Tsikos et al., 2003), reflecting oxidation and deposition of marine Mn(II). Planar Mn oxide laminae in the ~1.45 Ga Ullawarra Formation likely represent oxidized laminated Mn carbonates, though given the unavailability of unweathered samples this cannot be confirmed. The presence of laminated and planar bedded Mn siltstones exposed over ~90 km of strike (Figure 1) are still strong evidence of a sedimentary origin for these Mn deposits.

The carbon isotope data from Ilgarari Formation Mn carbonates are consistent with oxidation of organic matter (OM) via reduction of Mn(IV) oxides to Mn(II), yielding negative values for  $\delta^{13}\text{C}_{(\text{carbonate})}$  due to the incorporation of isotopically light OM-derived carbon into the Mn carbonates (Okita et al., 1988), as demonstrated by the negative values in the non-manganiferous OM-rich sections (Figures 3 and 5). Similar values are reported from other higher-grade primary sedimentary Mn deposits such as the Molango deposit in Mexico (Okita et al., 1988), the Usa deposit in Russia (Kuleshov & Bych, 2002), the Hotazel deposit in South Africa (Tsikos et al., 2003), and recent manganiferous sediments from the Baltic sea (Neumann et al., 2002). The Mn grades in our drill core analyses are lower than those large deposits (Figure 5); however, and this simply reflects the fact that our samples were collected from below the stratigraphic horizon of economic supergene mineralization in the Ilgarari Formation (Figure 6 and Appendix S1). Furthermore, our sampling was not biased toward Mn carbonate-rich bands (see example in Appendix S1), rather we sampled consistently every 5 m regardless of lithology or mineralogy.

Light  $\delta^{13}\text{C}_{(\text{carbonate})}$  values in Mn carbonate-bearing sediments have also been proposed to be possible by contribution of dissolved inorganic carbon (DIC) by aerobic oxidation of  $\text{CH}_4$  (methane) in anoxic ferruginous or suboxic conditions (Wittkop et al., 2020).

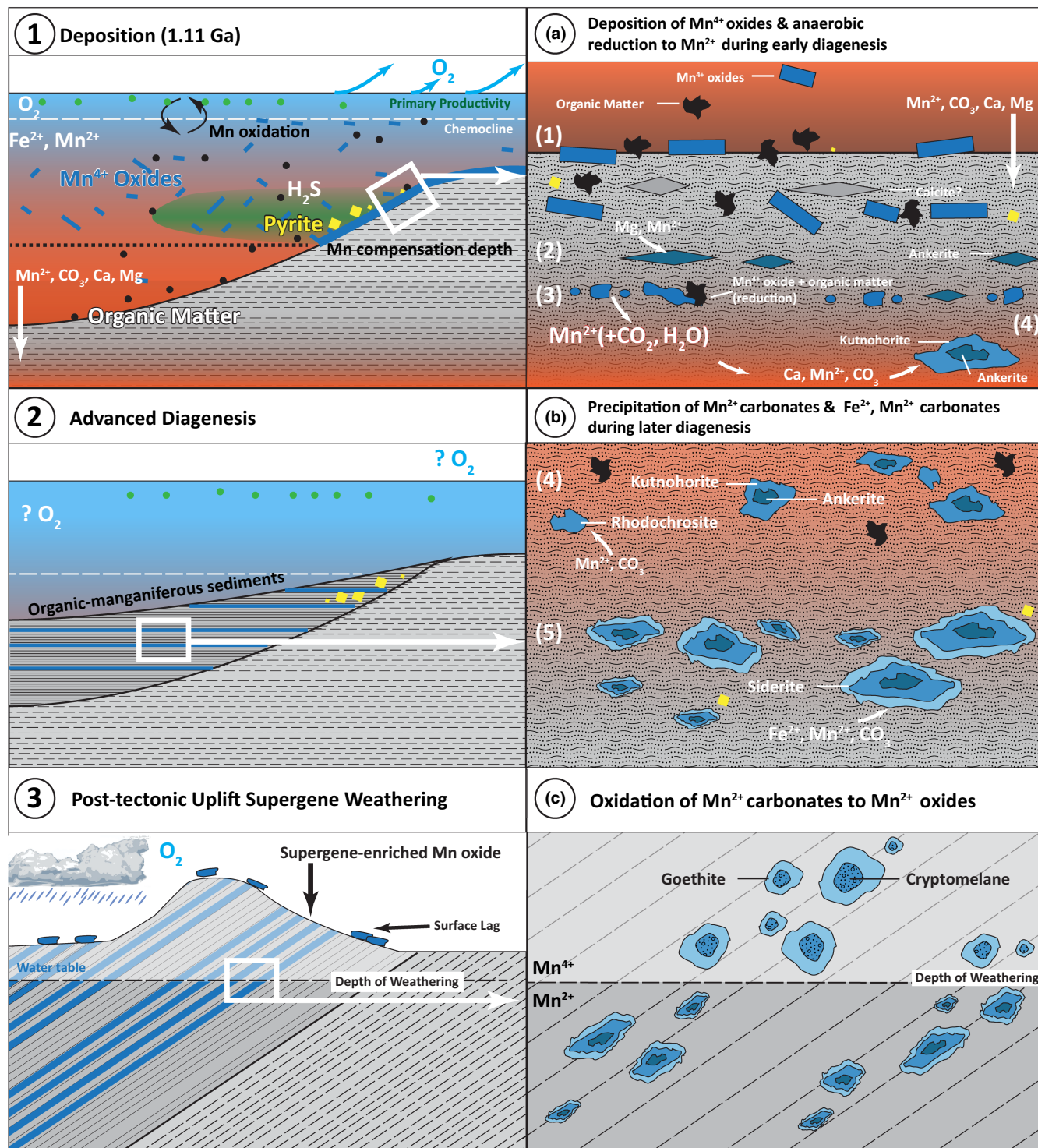


**FIGURE 6** Conceptual model of deposition of sedimentary manganese, diagenetic alteration, and supergene enrichment, as observed in the 1.1 Ga-hosted Butcherbird Mn deposit in the Ilgarari Fm. Step 1: Precipitation of  $Mn^{4+}$  oxides occurs as oxygenation of the upper water column commences and interacts with dissolved  $Mn^{2+}$  at the chemocline, and  $Mn^{4+}$  oxides are deposited as sediment. Detailed box a shows stages (1) deposition of  $Mn^{4+}$  oxides and organic matter, while dissolved  $Mn^{2+}$ ,  $CO_3$ , Ca, Mg descends into the porewater. (2) Early diagenetic carbonates (calcite) precipitate, and are later dolomitized to Mn-bearing ankerite with the addition of Mg and  $Mn^{2+}$ . (3) Sedimentary  $Mn^{4+}$  oxides are reduced by oxidation of organic matter, releasing  $Mn^{2+}$ . (4) Formation of microspheres by precipitation of kutnohorite with partial replacement of ankerite. Step 2: Advanced diagenesis. Detailed box b shows (4 cont.) kutnohorite continues to replace ankerite with contemporaneous precipitation of rhodochrosite where localized low Ca concentrations occur. (5) As Ca and  $Mn^{2+}$  concentrations are exhausted, Mn-bearing siderite precipitates on outer surface of microspheres. Step 3: Following lithification and uplift, oxidative weathering of the Ilgarari Fm occurs. Detailed box c shows the oxidation of the  $Mn^{2+}$  carbonate microspheres, preserving the microspheric textures. Ankerite and kutnohorite are converted to cryptomelane, with siderite rims converted to rims of goethite. The DD14IL014 drill hole studied here in Figure 3 and shown Figure S3 represents unaltered Ilgarari Formation sediments (bottom half of panel c and box c) whereas the supergene-enriched deposits shown in Figure 2b represent the top half of panel c and box c.

However, the authors of that study recognize that contribution of DIC by reduction of Mn oxide and sulfate via biologically mediated reduction of organic carbon are more thermodynamically favored than oxidation of methane. Given the abundance of pyrite observed there is a clear pathway for oxidation of organic carbon via sulfate reduction below the chemocline. Therefore, we interpret the Mn carbonates to record the deposition of authigenic Mn(IV) oxides from the water column, prior to reduction to Mn(II) via biologically mediated oxidation of organic carbon by reduction of Mn oxides and sulfate (Lovley & Phillips, 1988; Maynard, 2010) in the shallow subsurface, allowing Mn carbonates to precipitate (Figure 6).

## 5.2 | Cyclic oxygenation of the water column

The Fe chemistry of the Mn zones in the Ilgarari Formation suggest a close relationship between redox and Mn deposition, with corresponding cyclic variations in Mn carbonate concentration and ocean redox up section (Figure 3). The onset of Mn deposition in all 3 Mn Zones occurred in sediments with enrichments in highly reactive iron. We interpret this to reflect anoxia at the seabed allowing Mn(II) to accumulate beneath a redoxcline/chemocline, consistent with other studies that demonstrate oceanic anoxia in the Mesoproterozoic, e.g. Planavsky et al. (2011), but with progressive oxidation of Mn(II) at the redox interface. This implies the presence of oxygenated surface oceans interacting with a deeper dissolved reservoir of Mn(II). Following maximum Mn deposition, full oxidation of the water column followed, causing the cessation of Mn oxide deposition as the redoxcline and thus access to the Mn(II) reservoir would have been forced to deeper parts of the basin (Maynard, 2010). This cycle of Mn deposition and basin oxygenation was then repeated, forming the three observed Mn Zones (plus those zones present in the overlying weathered section). This redox cyclicity has been observed in the Baltic sea from the Holocene through to the present day where spatiotemporal variations in redox conditions in different positions and depths of the basin have led to enrichments in Mn and Fe (Hardisty et al., 2016, 2021; Scholz et al., 2013, 2018).

The redox geochemistry combined with sedimentological inferences imply oxygenated waters below the shelf break. Critically, these Ilgarari sediments were receiving relatively high organic carbon flux at these times (average TOC = 0.6% [max = 1.5%] for intervals between Mn zones). This stands in contrast to some other Mesoproterozoic settings that are interpreted to be oxygenated at depth, such as in the ~1.4 Ga Kaltasy Formation, central Russia (Sperling et al., 2014). Those sediments contain on average only 0.11% TOC, very low for basinal shales and implying oligotrophic surface water conditions and low export productivity. Since subsurface oxygen concentrations are the product of initial levels driven by atmospheric partial pressure minus organic carbon remineralization, weakly oxygenated deeper waters are still consistent with low atmospheric O<sub>2</sub> under conditions of low organic carbon export (e.g., in conditions where there has simply been very little oxygen loss)

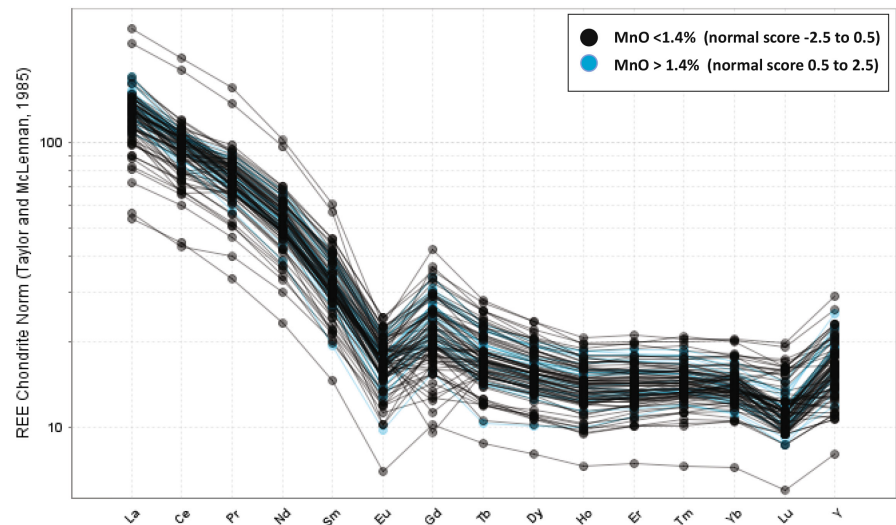
(Van de Velde et al., 2020). In contrast, the oxygenated Ilgarari sediments, with higher TOC levels, demand relatively higher levels of atmospheric oxygen.

## 5.3 | Oxidation-driven deposition of sedimentary manganese

Alternative oxidant pathways for the oxidation of Mn(II) to drive Mn deposition such as superoxide and other ROS, rather than free O<sub>2</sub>, have been demonstrated, e.g. Hansel (2017), and in many cases these may actually be the primary oxidant reacting with Mn(II). However, ROS also requires free oxygen for their formation; therefore, this oxidation pathway may act as a proxy for oxygenated (free O<sub>2</sub>) conditions. Light-driven anaerobic microbial oxidation of Mn(II) under strongly anoxic conditions has also been proposed as a possible pathway for Mn oxide deposition (Daye et al., 2019; Liu et al., 2020). Other pathways for Mn enrichments in anoxic conditions have also been proposed such as direct replacement of Ca carbonate by Mn carbonate in the presence of saturated Mn(II), but this likely also requires additional localized input of Mn(II) from reduction of sedimentary Mn oxides (Wittkop et al., 2020). Additionally, the potential for Mn oxidation at even low oxygen (sub- $\mu$ M) concentrations has been demonstrated in the heavily stratified modern Black Sea through the action of diverse Mn(II)-oxidizing enzymes in the sub-oxic zone (Clement et al., 2009). These alternative pathways for Mn enrichment in sedimentary rocks cast uncertainty on the robustness of Mn enrichments as independent proxies for oxidizing conditions in the ancient sedimentary rock record. However, even if these biologically mediated pathways for Mn oxidation had evolved in the late Mesoproterozoic, they do not account for the temporal distribution and transient occurrence of highly anomalous concentrations of Mn in marine sediments that are required to form giant, economically important Mn ore deposits. Rather, we consider ocean-atmosphere system redox changes to be more likely as the principal driver for deposition of such vast quantities of Mn. Furthermore, our Fe data that show cyclic oxygenation of the water column, independent of Mn enrichment, provides a good indicator that the main driver of Mn deposition in the Ilgarari Formation was oxidation of the basin ~1.1 Ga. The occurrence of the Mango Mn deposits in the ~1.4 Ga Ullawarra Formation in the Edmund Basin (Figure 1) is consistent with that observed in the Ilgarari Formation, and while we were unable to access unweathered material, we postulate that the stratiform Mn mineralization there is also sedimentary in origin. Widespread oxidative-driven Mn deposition in the Ilgarari Formation (1.11 Ga), and potentially in the Ullawarra Fm (1.45 Ga), thus adds to a growing collection of evidence for oxygenated surface environments at ~1.1 and 1.4 Ga (Canfield et al., 2018; Diamond & Lyons, 2018; Gilleaudeau et al., 2016; Gilleaudeau & Kah, 2015; Hardisty et al., 2017; Parnell et al., 2010, 2015; Sheen et al., 2018; Sperling et al., 2014; Wei et al., 2021; Zhang et al., 2018).

Oxidation of the water column alone does not account for the significant deposition of sedimentary Mn in the Edmund and Collier

**FIGURE 7** Spider plot of REE data from drill hole DD14IL014 showing prominent negative Eu anomaly. Note the same trend in Mn-anomalous and background samples.



groups; this also requires the presence of sufficient Mn(II) concentrations in the marine environment. This could be explained by the steady accumulation in the Mesoproterozoic marine Mn(II) reservoir during periods of low oxidation potential of the water column, but Maynard (2010) argued for Mn supply being a limiting factor for sedimentary Mn ore deposition through history, with hydrothermal vents being a viable source. Maynard (2010) suggested that positive Eu anomalies (normalized to chondritic REE values from Taylor & McLennan, 1985) were indicative of vent-proximal sourced Fe–Mn in sedimentary Mn deposits. There are no known hydrothermal conduit networks in the vicinity of the Butcherbird Mn deposit or proximal to the sampled drill hole. However, basin-scale hydrothermal sources of Mn should be considered, particularly given the fault/vein hosted Mn underlying the Woodie Woodie stratiform deposits. Our REE data normalized to chondritic REE values from Taylor and McLennan (1985) show a clear negative Eu anomaly (Figure 7). Maynard (2010) further suggests that Eu/Eu\* anomalies in the Archean–Paleoproterozoic Mn ores are high (>av. 0.93), whereas Mesoproterozoic and younger Mn deposits are lower with an average ~0.65. These trends are consistent with our data that have a mean Eu/Eu\* value of 0.63. Our REE data, when considered with the arguments of Maynard (2010) do not point toward vent-proximal sourced Mn in these deposits, but more likely reflect an enhanced/dynamically oxidized marine environment similar to that understood for the Neoproterozoic.

### 5.4 | Context of enhanced Mesoproterozoic sedimentary manganese

The total extent (tonnage) of the sedimentary Mn in the Edmund and Collier basins is not known, as only a small number of the hundreds of documented deposits and prospects have been measured in the Collier Basin and none in the Edmund Basin (Appendix S1). The known tonnage of the Collier Basin at ~1.1 Ga is at least 627 million tons (Mt) between the Collier and Manganese groups (7)

based on ore measurements from 9 Mn deposit camps (including Woodie Woodie, Appendix S1). The true extent, however, is clearly far higher given the hundreds of unmeasured deposits and prospects in the Collier Basin (Figure 1). This also applies to the Mn deposits of the Edmund Basin, which includes ~90 km of continually exposed stratiform Mn mineralization that form the Mango deposits (Figure 1, Appendix S1: Figure S5) but with no ore measurements. Combined minimum tonnages of Mn for the ~1.11 Ga Collier Group and Manganese Group of >627 Mt are commensurate with, if not greater than, the scale observed in many of the known Mn depositional periods of the Paleoproterozoic, and the main sedimentary Mn episodes of the Neoproterozoic and Phanerozoic (Figure 8). We can only speculate as to how significant the 1.45 Ga deposits are in terms of tonnage. Given their extent we can recognize that this likely represents a major Mn depositional event. If considered with the contemporaneous Wafangzi Mn deposit within the 1.46 Ga Tieling Formation in Northern China (Fan et al., 1999; Su et al., 2010), this indicates a significant and widespread Mn depositional event at that time. Therefore, our findings demonstrate that the Mesoproterozoic saw multiple episodes of sedimentary Mn deposition, a time otherwise considered a global “Mn hiatus.”

## 6 | CONCLUSION

Our data demonstrate that, contrary to previous assertions, widespread Mn deposition did indeed occur in the Mesoproterozoic oceans at 1.11 Ga, and likely at ~1.45 Ga. This occurred on a scale at least as significant as times throughout the Neoproterozoic and Phanerozoic following the second hypothesized oxygenation transition ~0.80 Ga (Johnson, Webb, et al., 2016; Maynard, 2010; Roy, 2006) and many periods during the Paleoproterozoic following the GOE (Figure 8). Given the broadly accepted links between sedimentary Mn deposition and free O<sub>2</sub> (Clement et al., 2009; Diem & Stumm, 1984; Johnson, Webb, et al., 2016; Maynard, 2010), coupled with our independent Fe data, we argue that this represents major

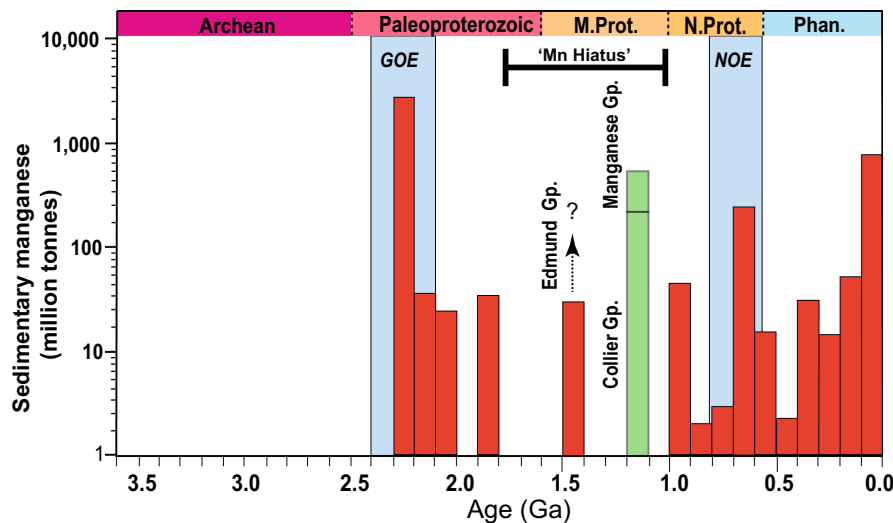


**FIGURE 8** Compilation of previously identified (red) sedimentary Mn deposits (million tons of Mn) throughout geological time (data modified from Maynard, 2010, Johnson, Webb, et al., 2016). The first major sedimentary Mn episode occurred during and following the GOE ~2.3 Ga, with the second major episode commencing on or before ~0.8 Ga close to the second major hypothesized oxygenation (NOE). A pronounced Mn hiatus in previously known Mn deposits occurs from the late Paleoproterozoic to the Neoproterozoic with the exception of the ~1.4 Ga Tieling Formation deposit in N. China (Fan et al., 1999; Su et al., 2010) and the Mango deposits in the Ullawarra Formation in the Edmund Group of Western Australia (Figure 1). Note there is no tonnage resource estimate for the Edmund Group Mn. The combined minimum tonnages of sedimentary Mn from the 1.1 Ga Collier and Manganese groups in Western Australia is shown in green, and exceed that of any period of the Neoproterozoic and most of the Paleoproterozoic and Phanerozoic.

widespread sedimentary Mn deposition that was a result of increased oxygenation of the surface environment at ~1.1 Ga, and potentially also at ~1.4 Ga. These results are consistent with an emerging model of transient oxidation in the Mesoproterozoic during those times and a more dynamic mid-Proterozoic Earth system than generally considered. Finally, these Western Australia Mn deposits require revision of statements regarding sedimentary manganese deposits through Earth's "middle age" (e.g., Cawood & Hawkesworth, 2014) irrespective of any ambiguities regarding depositional mechanism or absolute amount of oxygen available.

#### ACKNOWLEDGMENTS

We thank Austin Miller, Una Farrell, Derek Winchester, Tenten Pinchand, Mike Verrall, and Monica leGras for laboratory assistance, and the Geological Survey of Western Australia for assistance with access to the drill core. Helpful comments were given by Charlotte Stalvies and Chloe Plet (CSIRO). We also thank three anonymous reviewers, and handling Editors Kurt Konhauser and Tim Lyons, whose helpful comments improved the manuscript. The authors pay respect to the Whadjuk people of the Noongar Nation on which this manuscript was written.

#### FUNDING INFORMATION

This research was funded by the Australian Science and Industry Endowment Fund (SIEF) as part of The Distal Footprints of Giant Ore Systems: UNCOVER Australia Project (RP04-063)—Capricorn Distal Footprints. EAS also thanks the donors of The American Chemical Society Petroleum Research Fund for partial support of this research (61017-ND2).

#### CONFLICT OF INTEREST

None declared.

#### DATA AVAILABILITY STATEMENT

The data that supports the findings of this study are available in the Supplementary Material (Appendices S1 and S2, Tables S1 and S2) of this article.

#### ORCID

Sam C. Spinks <https://orcid.org/0000-0002-5794-6361>

Erik A. Sperling <https://orcid.org/0000-0001-9590-371X>

Robert L. Thorne <https://orcid.org/0000-0002-4200-6107>

Alistair J. R. White <https://orcid.org/0000-0003-3256-1171>

Joseph Armstrong <https://orcid.org/0000-0002-1342-3710>

Ian M. Tyler <https://orcid.org/0000-0003-1653-3939>

#### REFERENCES

- Alcott, L. J., Krause, A. J., Hammarlund, E. U., Bjerrum, C. J., Scholz, F., Xiong, Y., Hobson, A. J., Neve, L., Mills, B. J., März, C., Schnetger, B., Bekker, A., & Poulton, S. W. (2020). Development of iron speciation reference materials for Palaeoredox analysis. *Geostandards and Geoanalytical Research*, 44, 581–591.
- Armandola, S., Barham, M., Reddy, S. M., Clark, C., & Spinks, S. (2018). Footprint of a large intracontinental rifting event: Coupled detrital zircon geochronology and geochemistry from the Mesoproterozoic Collier Basin, Western Australia. *Precambrian Research*, 318, 156–169.
- Bellefroid, E. J., Hood, A. V. S., Hoffman, P. F., Thomas, M. D., Reinhard, C. T., & Planavsky, N. J. (2018). Constraints on Paleoproterozoic atmospheric oxygen levels. *Proceedings of the National Academy of Sciences of the United States of America*, 115, 8104–8109.

- Canfield, D. E., Poulton, S. W., Knoll, A. H., Narbonne, G. M., Ross, G., Goldberg, T., & Strauss, H. (2008). Ferruginous conditions dominated later Neoproterozoic deep-water chemistry. *Science*, *321*, 949–952.
- Canfield, D. E., Raiswell, R., Westrich, J. T., Reaves, C. M., & Berner, R. A. (1986). The use of chromium reduction in the analysis of reduced inorganic sulfur in sediments and shale. *Chemical Geology*, *54*, 149–155.
- Canfield, D. E., Zhang, S., Frank, A. B., Wang, X., Wang, H., Su, J., Ye, Y., & Frei, R. (2018). Highly fractionated chromium isotopes in Mesoproterozoic-aged shales and atmospheric oxygen. *Nature Communications*, *9*, 2871.
- Cawood, P. A., & Hawkesworth, C. J. (2014). Earth's middle age. *Geology*, *42*, 503–506.
- Cawood, P. A., & Tyler, I. M. (2004). Assembling and reactivating the Proterozoic Capricorn Orogen: Lithotectonic elements, orogenies, and significance. *Precambrian Research*, *128*, 201–218.
- Chen, X., Li, M., Sperling, E. A., Zhang, T., Zong, K., Liu, Y., & Shen, Y. (2020). Mesoproterozoic paleo-redox changes during 1500–1400 Ma in the Yanshan Basin, North China. *Precambrian Research*, *347*, 105835.
- Clement, B. G., Luther, G. W., & Tebo, B. M. (2009). Rapid, oxygen-dependent microbial Mn(II) oxidation kinetics at sub-micromolar oxygen concentrations in the Black Sea suboxic zone. *Geochimica et Cosmochimica Acta*, *73*, 1878–1889.
- Cole, D. B., Reinhard, C. T., Wang, X., Gueguen, B., Halverson, G. P., Gibson, T., Hodgskiss, M. S. W., McKenzie, N. R., Lyons, T. W., & Planavsky, N. J. (2016). A shale-hosted Cr isotope record of low atmospheric oxygen during the Proterozoic. *Geology*, *44*, 555–558.
- Crockford, P. W., Hayles, J. A., Bao, H., Planavsky, N. J., Bekker, A., Fralick, P. W., Halverson, G. P., Bui, T. H., Peng, Y., & Wing, B. A. (2018). Triple oxygen isotope evidence for limited mid-Proterozoic primary productivity. *Nature*, *559*, 613–616.
- Cutten, H., Johnson, S., Thorne, A., Wingate, M., Kirkland, C., Belousova, E., Blay, O., & Zwingmann, H. (2016). Deposition, provenance, inversion history and mineralization of the Proterozoic Edmund and Collier Basins, Capricorn Orogen. *Geological Survey of Western Australia Report*, *127*, 74.
- Daye, M., Klepac-Ceraj, V., Pajusalu, M., Rowland, S., Farrell-Sherman, A., Beukes, N., Tamura, N., Fournier, G., & Bosak, T. (2019). Light-driven anaerobic microbial oxidation of manganese. *Nature*, *576*, 311–314.
- Diamond, C. W., & Lyons, T. W. (2018). Mid-Proterozoic redox evolution and the possibility of transient oxygenation events. *Emerging Topics in Life Sciences*, *2*, 235–245.
- Diem, D., & Stumm, W. (1984). Is dissolved Mn<sup>2+</sup> being oxidized by O<sub>2</sub> in absence of Mn-bacteria or surface catalysts? *Geochimica et Cosmochimica Acta*, *48*, 1571–1573.
- Fan, D., Ye, J., & Li, J. (1999). Geology, mineralogy, and geochemistry of the Middle Proterozoic Wafangzi ferromanganese deposit, Liaoning Province, China. *Ore Geology Reviews*, *15*, 31–53.
- Freitas, B. T., Rudnitzki, I. D., Morais, L., Campos, M. D. R., Almeida, R. P., Warren, L. V., Boggiani, P. C., Caetano-Filho, S., Bedoya-Rueda, C., Babinski, M., Fairchild, T. R., & Trindade, R. I. F. (2021). Cryogenian glaciostatic and eustatic fluctuations and massive Marinoan-related deposition of Fe and Mn in the Urucum District, Brazil. *Geology*, *49*, 1478–1483.
- Geszvain, K., Butterfield, C., Davis, R. E., Madison, A. S., Lee, S.-W., Parker, D. L., Soldatova, A., Spiro, T. G., Luther, G. W., III, & Tebo, B. M. (2012). The molecular biogeochemistry of manganese(II) oxidation. *Biochemical Society Transactions*, *40*, 1244–1248.
- Gilleaudeau, G. J., Frei, R., Kaufman, A. J., Kah, L. C., Azmy, K., Bartley, J. K., Chernyavskiy, P., & Knoll, A. H. (2016). Oxygenation of the mid-Proterozoic atmosphere: Clues from chromium isotopes in carbonates. *Geochemical Perspectives Letters*, *2*(2), 178–187.
- Gilleaudeau, G. J., & Kah, L. C. (2015). Heterogeneous redox conditions and a shallow chemocline in the Mesoproterozoic Ocean: Evidence from carbon–sulfur–iron relationships. *Precambrian Research*, *257*, 94–108.
- Grey, K., Hocking, R., Stevens, M., Bagas, L., Carlsen, G., Irimes, F., Pirajno, F., Haines, P., & Apak, S. (2005). *Lithostratigraphic nomenclature of the Officer Basin and correlative parts of the Paterson Orogen, Western Australia*. Geological Survey of Western Australia Report. Geological Society of Western Australia.
- Grey, K., Yochelson, E. L., Fedonkin, M. A., & Martin, D. M. (2010). *Horodyskia williamsii* new species, a Mesoproterozoic macrofossil from Western Australia. *Precambrian Research*, *180*, 1–17.
- Hansel, C. M. (2017). Manganese in marine microbiology. *Advances in Microbial Physiology*, *70*, 37–83.
- Hardisty, D. S., Lu, Z., Bekker, A., Diamond, C., Gill, B., Jiang, G., Kah, L., Knoll, A., Loyd, S., Osburn, M. J., Planavsky, N., Wang, C., Zhou, X., & Lyons, T. (2017). Perspectives on Proterozoic surface ocean redox from iodine contents in ancient and recent carbonate. *Earth and Planetary Science Letters*, *463*, 159–170.
- Hardisty, D. S., Riedinger, N., Planavsky, N. J., Asael, D., Andren, T., Jorgensen, B. B., & Lyons, T. W. (2016). A Holocene history of dynamic water column redox conditions in the landsort Deep, Baltic Sea. *American Journal of Science*, *316*, 713–745.
- Hardisty, D. S., Riedinger, N., Planavsky, N. J., Asael, D., Bates, S. M., & Lyons, T. W. (2021). Holocene spatiotemporal redox variations in the southern Baltic Sea. *Frontiers in Earth Sciences*, *9*, 671401.
- Hodgskiss, M. S. W., & Sperling, E. A. (2022). A prolonged, two-step oxygenation of Earth's early atmosphere: Support from confidence intervals. *Geology*, *50*, 158–162.
- Johnson, J. E., Savalia, P., Davis, R., Kocar, B. D., Webb, S. M., Neelson, K. H., & Fischer, W. W. (2016). Real-time manganese phase dynamics during biological and abiotic manganese oxide reduction. *Environmental Science & Technology*, *50*, 4248–4258.
- Johnson, J. E., Webb, S. M., Ma, C., & Fischer, W. W. (2016). Manganese mineralogy and diagenesis in the sedimentary rock record. *Geochimica et Cosmochimica Acta*, *173*, 210–231.
- Johnson, J. E., Webb, S. M., Thomas, K., Ono, S., Kirschvink, J. L., & Fischer, W. W. (2013). Manganese-oxidizing photosynthesis before the rise of cyanobacteria. *Proceedings of the National Academy of Sciences of the United States of America*, *110*, 11238–11243.
- Jones, S., McNaughton, N. J., & Grguric, B. (2013). Structural controls and timing of fault-hosted manganese at Woodie, East Pilbara, Western Australia. *Ore Geology Reviews*, *50*, 52–82.
- Jones, S. A. (2017). Geology and geochemistry of fault-hosted hydrothermal and sedimentary manganese deposits in the Oakover Basin, east Pilbara, Western Australia. *Australian Journal of Earth Sciences*, *64*, 63–102.
- Kuleshov, V., & Bych, A. (2002). Isotopic composition ( $\delta^{13}\text{C}$ ,  $\delta^{18}\text{O}$ ) and origin of manganese carbonate ores of the Usa deposit (Kuznetskii Alatau). *Lithology and Mineral Resources*, *37*, 330–343.
- Learman, D. R., Voelker, B. M., Vazquez-Rodriguez, A. I., & Hansel, C. M. (2011). Formation of manganese oxides by bacterially generated superoxide. *Nature Geoscience*, *4*, 95–98.
- Liu, W., Hao, J., Elzinga, E. J., Piotrowiak, P., Nanda, V., Yee, N., & Falkowski, P. G. (2020). Anoxic photogeochemical oxidation of manganese carbonate yields manganese oxide. *Proceedings of the National Academy of Sciences of the United States of America*, *117*, 22698–22704.
- Liu, X.-M., Kah, L. C., Knoll, A. H., Cui, H., Wang, C., Bekker, A., & Hazen, R. M. (2021). A persistently low level of atmospheric oxygen in Earth's middle age. *Nature Communications*, *12*, 351.
- Lovley, D. R., & Phillips, E. J. P. (1988). Novel mode of microbial energy metabolism: Organic carbon oxidation coupled to dissimilatory reduction of iron or manganese. *Applied and Environmental Microbiology*, *54*, 1472–1480.
- Lyons, T. W., Reinhard, C. T., & Planavsky, N. J. (2014). The rise of oxygen in Earth's early ocean and atmosphere. *Nature*, *506*, 307–315.

- Martin, D. M., Sheppard, S., & Thorne, A. M. (2005). Geology of the Maroonah, Ullawarra, Capricorn, Mangaroon, Edmund, and Elliott Creek 1:100,000 sheets. 1:100,000 Geological Series Explanatory Notes.
- Martin, D. M., Sircombe, K. N., Thorne, A. M., Cawood, P. A., & Nemchin, A. A. (2008). Provenance history of the Bangemall Supergroup and implications for the Mesoproterozoic paleogeography of the West Australian Craton. *Precambrian Research*, 166, 93–110.
- Martin, D. M., & Thorne, A. M. (2004). Tectonic setting and basin evolution of the Bangemall supergroup in the northwestern Capricorn Orogen. *Precambrian Research*, 128, 385–409.
- Maynard, J. B. (2010). The chemistry of manganese ores through time: A signal of increasing diversity of earth-surface environments. *Economic Geology*, 105, 535–552.
- Neumann, T., Heiser, U., Leosson, M. A., & Kersten, M. (2002). Early diagenetic processes during Mn-carbonate formation: Evidence from the isotopic composition of authigenic Ca-rhodochrosites of the Baltic Sea. *Geochimica et Cosmochimica Acta*, 66, 867–879.
- Okita, P. M., Maynard, J. B., Spiker, E. C., & Force, E. R. (1988). Isotopic evidence for organic matter oxidation by manganese reduction in the formation of stratiform manganese carbonate ore. *Geochimica et Cosmochimica Acta*, 52, 2679–2685.
- Parnell, J., Boyce, A. J., Mark, D., Bowden, S., & Spinks, S. (2010). Early oxygenation of the terrestrial environment during the Mesoproterozoic. *Nature*, 468, 290–293.
- Parnell, J., Spinks, S., Andrews, S., Thayalan, W., & Bowden, S. (2015). High molybdenum availability for evolution in a Mesoproterozoic lacustrine environment. *Nature Communications*, 6, 6996.
- Pirajno, F., Mernagh, T. P., Huston, D., Creaser, R. A., & Seltmann, R. (2016). The Mesoproterozoic Abra polymetallic sedimentary rock-hosted mineral deposit, Edmund Basin, Western Australia. *Ore Geology Reviews*, 76, 442–462.
- Planavsky, N. J., Asael, D., Hofmann, A., Reinhard, C. T., Lalonde, S. V., Knudsen, A., Wang, X., Ossa, F., Pecoits, E., Smith, A. J. B., Beukes, N. J., Bekker, A., Johnson, T. M., Konhauser, K. O., Lyons, T. W., & Rouxel, O. J. (2014). Evidence for oxygenic photosynthesis half a billion years before the great oxidation event. *Nature Geoscience*, 7, 283–286.
- Planavsky, N. J., Cole, D. B., Isson, T. T., Reinhard, C. T., Crockford, P. W., Sheldon, N. D., & Lyons, T. W. (2018). A case for low atmospheric oxygen levels during Earth's middle history. *Emerging Topics in Life Sciences*, 2, 149–159.
- Planavsky, N. J., McGoldrick, P., Scott, C. T., Li, C., Reinhard, C. T., Kelly, A. E., Chu, X., Bekker, A., Love, G. D., & Lyons, T. W. (2011). Widespread iron-rich conditions in the mid-Proterozoic ocean. *Nature*, 477, 448–451.
- Planavsky, N. J., Reinhard, C. T., Wang, X., Thomson, D., McGoldrick, P., Rainbird, R. H., Johnson, T., Fischer, W. W., & Lyons, T. W. (2014). Low mid-Proterozoic atmospheric oxygen levels and the delayed rise of animals. *Science*, 346, 635–638.
- Poulton, S. W., Bekker, A., Cumming, V. M., Zerkle, A. L., Canfield, D. E., & Johnston, D. T. (2021). A 200-million-year delay in permanent atmospheric oxygenation. *Nature*, 592, 232–236.
- Poulton, S. W., & Canfield, D. E. (2005). Development of a sequential extraction procedure for iron: Implications for iron partitioning in continentally derived particulates. *Chemical Geology*, 214, 209–221.
- Poulton, S. W., & Canfield, D. E. (2011). Ferruginous conditions: A dominant feature of the ocean through Earth's history. *Elements*, 7, 107–112.
- Raiswell, R., & Canfield, D. E. (1998). Sources of iron for pyrite formation in marine sediments. *American Journal of Science*, 298, 219–245.
- Raiswell, R., Hardisty, D. S., Lyons, T. W., Canfield, D. E., Owens, J. D., Planavsky, N. J., Poulton, S. W., & Reinhard, C. T. (2018). The iron paleoredox proxies: A guide to the pitfalls, problems and proper practice. *American Journal of Science*, 318, 491–526.
- Roy, S. (2006). Sedimentary manganese metallogenesis in response to the evolution of the Earth system. *Earth-Science Reviews*, 77, 273–305.
- Scholz, F., Baum, M., Siebert, C., Eroglu, S., Dale, A. W., Naumann, M., & Sommer, S. (2018). Sedimentary molybdenum cycling in the aftermath of seawater inflow to the intermittently euxinic Gotland Deep, Central Baltic Sea. *Chemical Geology*, 491, 27–38.
- Scholz, F., McManus, J., & Sommer, S. (2013). The manganese and iron shuttle in a modern euxinic basin and implications for molybdenum cycling at euxinic ocean margins. *Chemical Geology*, 355, 56–68.
- Scott, C., & Lyons, T. W. (2012). Contrasting molybdenum cycling and isotopic properties in euxinic versus non-euxinic sediments and sedimentary rocks: Refining the paleoproxies. *Chemical Geology*, 324, 19–27.
- Sheen, A. I., Kendall, B., Reinhard, C. T., Creaser, R. A., Lyons, T. W., Bekker, A., Poulton, S. W., & Anbar, A. D. (2018). A model for the oceanic mass balance of rhenium and implications for the extent of Proterozoic ocean anoxia. *Geochimica et Cosmochimica Acta*, 227, 75–95.
- Sheppard, S., Occhipinti, S., & Nelson, D. (2005). Intracontinental reworking in the Capricorn Orogen, Western Australia: The 1680–1620 Ma Mangaroon Orogeny. *Australian Journal of Earth Sciences*, 52, 443–460.
- Slotznick, S. P., Sperling, E. A., Tosca, N. J., Miller, A. J., Clayton, K. E., van Helmond, N. A. G. M., Slomp, C. P., & Swanson-Hysell, N. L. (2020). Unraveling the mineralogical complexity of sediment iron speciation using sequential extractions. *Geochemistry, Geophysics, Geosystems*, 21, e2019GC008666.
- Sperling, E. A., Carbone, C., Strauss, J. V., Johnston, D. T., Narbonne, G. M., & Macdonald, F. A. (2016). Oxygen, facies, and secular controls on the appearance of Cryogenian and Ediacaran body and trace fossils in the Mackenzie Mountains of northwestern Canada. *Geological Society of America Bulletin*, 128, 558–575.
- Sperling, E. A., Melchin, M. J., Fraser, T., Stockey, R. G., Farrell, U. C., Bhajan, L., Brunoir, T. N., Cole, D. B., Gill, B. C., Lenz, A., Loydell, D. K., Malinowski, J., Miller, A. J., Plaza-Torres, S., Bock, B., Rooney, A. D., Tecklenburg, S. A., Vogel, J. M., Planavsky, N. J., & Strauss, J. V. (2021). A long-term record of early to mid-Paleozoic marine redox change. *Science Advances*, 7, eabf4382.
- Sperling, E. A., Rooney, A. D., Hays, L., Sergeev, V. N., Vorob'eva, N. G., Sergeeva, N. D., Selby, D., Johnston, D. T., & Knoll, A. H. (2014). Redox heterogeneity of subsurface waters in the Mesoproterozoic ocean. *Geobiology*, 12, 373–386.
- Spinks, S. C., Uvarova, Y., Thorne, R., Anand, R., Reid, N., White, A., Ley-Cooper, Y., Bardwell, N., Gray, D., Meadows, H., & LeGras, M. (2017). Detection of zinc deposits using terrestrial ferromanganese crusts. *Ore Geology Reviews*, 80, 484–503.
- Stookey, L. L. (1970). Ferrozine – A new spectrophotometric reagent for iron. *Analytical Chemistry*, 42, 779–781.
- Su, W., Li, H., Huff, W. D., Ethensohn, F. R., Zhang, S., Zhou, H., & Wan, Y. (2010). SHRIMP U-Pb dating for a K-bentonite bed in the Tieling Formation, North China. *Chinese Science Bulletin*, 55, 3312–3323.
- Taylor, S. R., & McLennan, S. M. (1985). *The continental crust: Its composition and evolution* (pp. 1–312). Blackwell Scientific Publications.
- Tebo, B. M., Geszvain, K., & Lee, S.-W. (2010). The molecular geomicrobiology of bacterial manganese(II) oxidation. In L. L. Barton, M. Mandl, & A. Loy (Eds.), *Geomicrobiology: Molecular and environmental perspective* (pp. 285–308). Springer.
- Thorne, A. (2018). *Ullawarra Formation (P<sub>1</sub>-MEI-s1): Geological Survey of Western Australia, Explanatory Notes Extract*. <https://www.dmp.wa.gov.au/ens>
- Tsikos, H., Beukes, N. J., Moore, J. M., & Harris, C. (2003). Deposition, diagenesis, and secondary enrichment of metals in the Paleoproterozoic Hotazel Iron Formation, Kalahari Manganese Field, South Africa. *Economic Geology*, 98, 1449–1462.

- Van Cappellen, P., Viollier, E., Roychoudhury, A., Clark, L., Ingall, E., Lowe, K., & Dichristina, T. (1998). Biogeochemical cycles of manganese and iron at the oxic-anoxic transition of a stratified Marine Basin (Orca Basin, Gulf of Mexico). *Environmental Science & Technology*, 32, 2931–2939.
- Van de Velde, S. J., Reinhard, C. T., Ridgwell, A., & Meysman, F. J. R. (2020). Bistability in the redox chemistry of sediments and oceans. *Proceedings of the National Academy of Sciences of the United States of America*, 117, 33043–33050.
- Wei, W., Frei, R., Kläbe, R., Tang, D., Wei, G.-Y., Li, D., Tian, L.-L., Huang, F., & Ling, H.-F. (2021). A transient swing to higher oxygen levels in the atmosphere and oceans at ~1.4 Ga. *Precambrian Research*, 354, 106058.
- Wingate, M. T. D., Creaser, R. A., Lu, Y., Spinks, S., & Cutten, H. N. (2021). 217288: *Black shale, Irregully Creek (Blue Billy Formation, Edmund Group, Bangemall Supergroup, Capricorn Orogen)*. *Geochronology Record*.
- Wittkop, C., Swanner, E. D., Grengs, A., Lambrecht, N., Fakhraee, M., Myrbo, A., Bray, A. W., Poulton, S. W., & Katsev, S. (2020). Evaluating a primary carbonate pathway for manganese enrichments in reducing environments. *Earth and Planetary Science Letters*, 538, 116201.
- Zhang, K., Zhu, X., Wood, R. A., Shi, Y., Gao, Z., & Poulton, S. W. (2018). Oxygenation of the Mesoproterozoic ocean and the evolution of complex eukaryotes. *Nature Geoscience*, 11, 345–350.
- Zhang, S., Wang, X., Wang, H., Bjerrum, C. J., Hammarlund, E. U., Costa, M. M., Connelly, J. N., Zhang, B., Su, J., & Canfield, D. E. (2016).

Sufficient oxygen for animal respiration 1,400 million years ago. *Proceedings of the National Academy of Sciences of the United States of America*, 113, 1731–1736.

- Zhang, S., Wang, X., Wang, H., Hammarlund, E. U., Su, J., Wang, Y., & Canfield, D. E. (2017). The oxic degradation of sedimentary organic matter 1400 Ma constrains atmospheric oxygen levels. *Biogeosciences*, 14, 2133–2149.

## SUPPORTING INFORMATION

Additional supporting information can be found online in the Supporting Information section at the end of this article.

**How to cite this article:** Spinks, S. C., Sperling, E. A., Thorne, R. L., LaFountain, F., White, A. J. R., Armstrong, J., Woltering, M., & Tyler, I. M. (2023). Mesoproterozoic surface oxygenation accompanied major sedimentary manganese deposition at 1.4 and 1.1 Ga. *Geobiology*, 21, 28–43. <https://doi.org/10.1111/gbi.12524>